Available online at www.sciencedirect.com
SCIENCE DIRECT®
Nuclear Instruments and Methods in Physics Research B 244 (2006) 307–322
NIM B
Beam Interactions with Materials & Atoms
www.elsevier.com/locate/nimb

e-Induced secondary electron emission yield of insulators and charging effects

J. Cazaux *

LASSI/UTAP, Faculté des Sciences, Universite de Reims (DTI/CNRS), B.P. 1039, 51687 Reims Cedex 2, France

Received 5 July 2005; received in revised form 20 September 2005
Available online 22 November 2005

Abstract

Based on a more realistic description of the in-depth secondary electron generation than that of standard (constant loss) model, a new model for the e-induced secondary electron emission yield, $\delta = f(E^0)$, is applied to account for the observed mean atomic number dependence of the reduced yield curves (RYC), $\delta/\delta_{max} = f(E^0/E^0_{max})$ of a wide variety of inorganic insulators. It is next used to extract and to discuss physical information on secondary electron escape probability and attenuation length of a number of oxides and alkali halides and to deduce their X-ray-induced secondary electron emission yield, $\delta^X = f(h\nu)$. Extrapolation of experimental data above the few keV energy range including the estimate of the nominal critical energy E^0_2 is also illustrated. Correlation between time dependence of charging and of secondary electron emission is next analyzed and various charging effects such as the observed negative charging when a positive charging was expected or the possible change of sign of the specimen current, are explained by the difference between E^0_2 and E^C_2 (critical energy obtained under permanent irradiation). Strategies to identify charging effects via their influence on the distortion of the yield curve and to reduce them are finally suggested.

PACS: 79.20.Hx; 61.82.Ms; 61.80.Cb; 61.16.Bg

Keywords: Secondary electron emission; Insulators; Charging; Electron transport; X-ray induced secondary electron emission; Scanning electron microscopy

1. Introduction

There has been much work on the electron-induced secondary electron emission (e-SEE) from inorganic insulators [1–5] and this attention continues nowadays because of its important role in many fields of modern technology such as in insulator breakdown (damaging electronic devices) and in electron lithography as well as in the behaviour of space aircrafts and interstellar dust grains submitted to cosmic radiation [6,7]. When submitted to electron irradiation, these materials are characterized by their efficient SEE property but strongly disturbed by charging effects and these effects are also the major impediment to a successful investigation of these materials in techniques based on the SE emission such as scanning electron microscopy [8].

The aim of the present contribution is first to deal with normal yield curves (NYC), $\delta = f(E^0)$, and reduced yield curves RYC, $\delta/\delta_{max} = f(E^0/E^0_{max})$ of a wide variety of inorganic insulators in order to identify the key parameters governing their SEE yield when short pulsed excitations are used for preventing charging. Next the influence of charging on these yields is investigated in order to deduce strategies for minimizing its effects.

For the first goal, the use of more or less sophisticated Monte Carlo simulations is possible [9–12] but this use is often restricted to only one compound and the common points between compounds belonging to the wide class of inorganic insulators cannot appear clearly. Also results are scarcely compared to experiments. On the contrary, for practical purposes, the interpretation of experimental

* Tel.: +33 326 042 137/913 223; fax: +33 326 913 300/312.
E-mail address: jacques.cazaux@univ-reims.fr

0168-583X/$ - see front matter © 2005 Elsevier B.V. All rights reserved.
doi:10.1016/j.nimb.2005.10.006

results is generally based on the use of simple analytical forms derived from the constant loss model (referred to below as the standard model) [3,5,13–15] but fitting procedures between calculations and experiments requires an arbitrary change of the exponent '*n*' in a ''universal'' power law expression relating the primary electron range, R, to the primary energy, E^0. To avoid such an arbitrary choice, the present analytical approach tries to keep the simplicity of standard model but with a more realistic description for the SE in-depth generation in the materials of interest. Here, its simplicity allows it to apply to a large number of published data in order to evaluate and to discuss the relative weight of the relevant parameters involved in the three-step process of SEE: generation; transport and escape.

Focussed on the distortion of the secondary yield curves of insulators during irradiation, the second goal is attained by correlating the time dependence of charging mechanisms to the time evolution of parameters involved in the SEE process and SE collection. A special attention is devoted to the difference between the nominal critical energy E_2^0 under uncharged conditions and the experimental critical energy E_2^C attained under permanent irradiation. Strategies to minimize charging effects or to identify them are indicated. In particular any deviation between experiments and calculations derived from the suggested model permits to suspect the reliability of experimental results.

2. Analysis of experimental results with standard model

2.1. Experimental normal yield curves (NYC) and reduced yield curves (RYC)

In many experiments the measurement of the SEE yield, δ, includes in fact the contribution of the backscattering coefficient, η. This convention is kept in this section and in the next one but η is explicitly indicated in the section devoted to charging. Also the present investigation is restricted to normal incidence on thick samples.

The analysis of a rather large number of published data, $\delta = f(E^0)$, obtained on a wide variety of alkali halides and metallic oxides [16–22] and a very useful database [23] shows that the maximum yield, δ_{max}, of most of inorganic insulators is one order of magnitude larger than that of metals (or more) but there are large deviations between experimental results obtained by different authors as well as results obtained by the same authors on different samples having a common chemical composition. For instance for KBr, Whetten [17] finds a maximum value, $\delta_{max} \sim 14$ (at $E^0_{max} \sim 2.1$ keV) for cleaved crystals and $\sim$12 (at 1.8 eV) for evaporated KBr specimens while, for the same compound, KBr, Petzel [16] reports the decrease of δ_{max} from 12.5 (at 1.5 keV) to 10.8 (at 1.25 keV) when the temperature increases from 35 to 300 °C. For the most widely investigated insulator, MgO, the deviations are much more important: $\delta_{max} \sim 3.4$ and 3.6 (at 0.75 and 1.1 keV) for films prepared by electron beam evaporation on a non-heated (S1) and heated (S2) Si substrate [19]; $\delta_{max} \sim 7.1$ and $\sim$6.2 (the two at $E^0_{max} \sim 1$ keV), for single crystals at room temperature and at 740 °C [20]; $\delta_{max} \sim 19.5$ and 24.6 (at 1.1 and 1.3 keV) for, respectively, a thin film and a single crystal [17]. Discussed in Section 3.3 and illustrated below in Fig. 5, these large deviations, $3.4 \leqslant \delta_{max} \leqslant 24.6$ (with $0.65\ \text{keV} \leqslant E^0_{max} \leqslant 1.3\ \text{keV}$), are far larger than the experimental uncertainties and they cannot be attributed to systematic errors or to charging effects (see below Section 4). Such large deviations explain the difficulty to predict the yield of a given insulator from only its chemical composition and it also explain the frequent lack of comparison between sophisticated simulations and experimental results. For a given compound, these deviations disappear when experiments are displayed in the form of reduced yield results obtained by dividing each measured yield, δ, by the corresponding δ_{max} value, also dividing E^0 by E^0_{max}. Fig. 1(a) for KBr and in Fig. 1(b) for MgO show that all the experimental points are located on or close to a curve labelled $k = 1/3$ for KBr and $k = 0.45$ for MgO. In contrast to NYC, $\delta = f(E^0)$, the obtained RYC, δ/δ_{max} versus E^0/E^0_{max}, are characteristic of the chemical composition of the compound of interest independently of its temperature, crystalline state and elaboration process. Fig. 2 shows the results of the same normalization process applied to data obtained on various alkali halides (LiF; KCl and KI cleaved crystals and a non-cleaved CaF_2 crystal [17]) and on various oxides (two varieties of Al_2O_3 [21]; two varieties of BeO [22]; an amorphous wet SiO_2 specimen [24] and a mica [25]). Driven by the need to cover the largest mean atomic number range as possible, the result obtained on platinum [26], $Z = 78$, is also shown. Like for KBr and MgO, the difference between the various initial data obtained on a given compound disappear when experimental results are expressed in the form of RYC. The RYCs of two varieties of alumina are very similar to that of MgO and they are closed to each other despite the difference between their maximum values: $\delta_{max} \sim 6.4$ (at 0.6 keV) on as-received sapphire and $\sim$7.8 (at 0.65 keV) on a highly polished single crystal of Al_2O_3; the RYCs of two varieties of BeO, bare BeO and ceasiated surface BeO, are also quite superimposed despite their differences for their E^0_{max} values (0.36 and 0.42 keV) and their δ_{max} values (4 and 6.5) [22]. Not shown in Fig. 2 for clarity, the reduced yield results of two other variety of SiO_2 samples, quartz [27] and glass [28], also fit, within the experimental uncertainties, the result obtained on a wet form of amorphous SiO_2 [24]. The significant difference in the evolution of the reduced yield results when going from BeO or LiF up to Pt is also clear in Fig. 2 but to be unambiguous, these differences with mean atomic number, $\langle Z \rangle$, require the exploration of the largest reduced energy range, E^0/E^0_{max}, as possible because the normalization procedure obviously leads all the evolutions to pass by a common point, $\delta/\delta_{max} = 1$ at $E^0/E^0_{max} = 1$. An excellent precision is also required for δ_{max} and E^0_{max} values because they define the reduced units. Consequently, a rather large number of

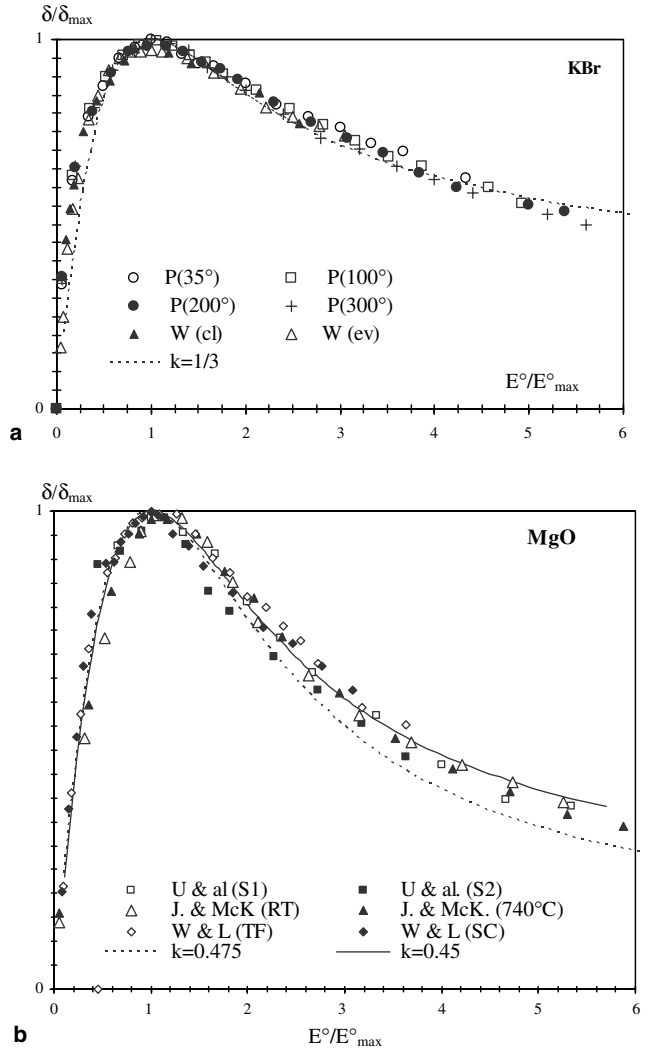

Fig. 1. Reduced yield results, symbols, deduced from experiments for KBr (a) and for MgO (b). For KBr, initial data are from [16] at different temperatures, P(35°) to P(300°), and from [17] for a cleaved and an evaporated specimen, respect: W(cl) and W(ev). For MgO, initial data are from [19] for specimens obtained on a non-heated, (U & al. S1), and a heated substrate, (U & al. S2); from [20], (J & McK room temperature – RT – and 740 °C), and from [18] on a thin film, W&L (TF), and on a single crystal W&L (SC). Curves $k = 1/3$ for KBr; $k = 0.45$ and 0.475 for MgO are calculated from Eq. (5).

experimental points at around the maximum of the initial yield data have to be acquired and the use of modern automatic acquisition systems (such as that operated for BeO [22] or Pt [26]) is highly recommended.

2.2. Standard model

The standard model is the simplest model to describe SE emission and to interpret the SEE experimental results [3,14,15,29]. Its basic assumption is to consider that the energy dissipation of primary electrons, PE, within the material is a constant in depth, z, down to their range R

$$E(z)\mathrm{d}z = (E^0/R)\mathrm{d}z, \tag{1}$$

where $E(z)\mathrm{d}z$ is the energy lost by one PE between z and $z + \mathrm{d}z$. Next postulating a one-dimensional exponential attenuation function, $\exp -z/s$, for the SE transport towards the surface (s: SE attenuation length) and a constant, A, for the SE escape probability into the vacuum, the final expression is:

$$\delta = A[E^0/E_{se}]\alpha^{-1}(1 - \mathrm{e}^{-\alpha}) \tag{2}$$

with $\alpha = R/s$. The mean energy required to produce a SE is E_{se} and it corresponds to $n_{se} = E^0/E_{se}$ with n_{se} = total number of SE generated (per incident PE).

To be useful, Eq. (2) needs to be combined to an energy-range relationship, $R = f(E^0)$. Many expressions have been suggested. All take the general form [30]:

$$R\ (\mathrm{nm}) = CE^{0n}\ (\mathrm{keV}). \tag{3}$$

Unfortunately, they differ from each other by the values of the exponent n and of the material constant C. For instance, for Fitting [31] it is $n = 1.3$ and $C = 90/\rho^{0.8}$ for $E^0 < 10$ keV with ρ: mass density in g/cm^3; for Kanaya and Kawakatsu [32], it is $n = 4/3$ for 0.8 keV $< E^0 <$ 2 keV and $n = 1.5$ for 2 keV $< E^0 <$ 10 keV with different C values. For the direct interpretation of SEE yield data, the most frequent choice is $n = 1.35$ and $C = 115/\rho$ [14,15,29,33] but Burke [34] suggested an empirical value $n = 1.725$ for polymers when $n = 1.4$ was suggested by Grais and Bastawros [5] for insulators and semiconductors. The evidence is that no truly universal curve exists [35] but physical arguments are missing for the best choice of a single value for n.

The same evidence may be seen in Fig. 2 where the RYC (full lines) have been calculated from Eqs. 2 and 3 for exponent values ranging from $n = 1.3$ up to $n = 2$. For such calculations, the evolution of $\delta E_{se}/A$ as a function of increasing values of $\alpha^{1/n}$ are evaluated with $E^0 = (s\alpha/C)^{1/n}$. This evolution passes by a maximum and the two coordinates of this maximum are normalized to the unity by setting δ_{max} $E_{se}/A = 1$ and $\alpha_{max}^{1/n} = (C/s)^{1/n}E_{max}^0 = 1$.

3. A new model and selected applications

3.1. Overview of a new model

A more physical approach than that used in standard model is to reconsider the hypothesis of Eq. (1) following which the energy dissipation of incident electrons is a constant in depth for $0 \leqslant z \leqslant R$. For this, inspired from the point source diffusion model [32,36,37], the new model supposes that the incident electrons travel straight into the target up to the depth of complete diffusion after which they diffuse isotropically in all directions. The irradiated volume has the shape of a truncated sphere centred at a point C more or less closer to the surface depending upon the $\langle Z \rangle$ value of the target material. For large atomic numbers the diffusion depth is so small that the incident electrons diffused almost immediately and the diffusion depth increases when $\langle Z \rangle$ decreases. Then, this new model

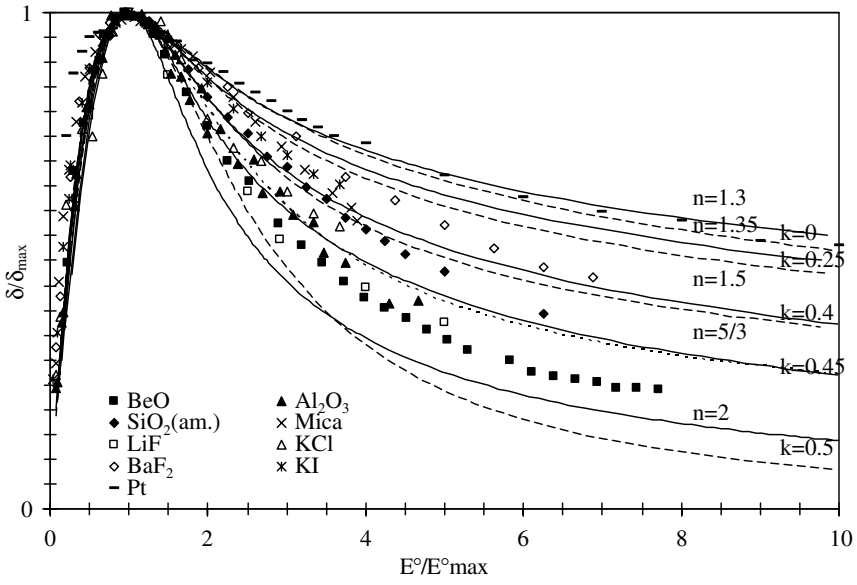

Fig. 2. Reduced yield results of some other oxides and alkali halides. The initial data are that of BeO [22]; SiO_2 [24]; mica [25]; LiF; KCl; KI and BaF_2 [17] and results on Pt are given for a comparison [26]. Full lines: calculations from standard model, Eq. (2) with exponent n (Eq. (3)) ranging from $n = 1.3$ (top) to $n = 2$ (bottom). Dashed lines: calculations from present model, Eq. (5) with parameter k ranging from $k = 0$ (top) to $k = 0.5$ (bottom) and $n = 1.35$.

postulates a uniform SE generation inside the irradiated truncated spherical volume with a centre, C, located at the most probable energy dissipation depth, z_C. The relative position of C is $k = z_C/R$, where k is nearly zero for large atomic number and it is near from $k = 0.4$–0.5 for ultra light materials [38,39]. In present model, the energy dissipation (per unit depth) of one PE, $E(z)$ is now:

$$E(z)\mathrm{d}z = E^0[3/(2-3k)][1/R^2][(R-z_C)^2 - (z_C - z)^2]\,\mathrm{d}z. \tag{4}$$

In fact the parabolic in-depth generation of the SEs of Eq. (4) applies to irradiated volumes having either the shape of truncated spheres or truncated ellipsoids (see right inset of Fig. 3 and [38] for details) and, as it may be seen in Fig. 3, it is consistent with experimental results obtained at 5 and 12 keV for air [40].

Next, similarly to standard model, an exponential attenuation function, $\exp -z/s$, for the SE transport and a parameter, A, for the SE escape probability are chosen to obtain, after integration, the key expression of present model:

$$\delta = [AE^0/E_{se}][3/(2-3k)]\alpha^{-1}[D+F] \tag{5}$$

with $D = 1 - 2\mathrm{k} + 2\mathrm{k}\alpha^{-1} - 2\alpha^{-2}$; $F = 2\alpha^{-1} - \mathrm{k} + \alpha^{-1}\mathrm{e}^{-\alpha}$ and again $\alpha = R/s$.

This approach permits to choose a unique value for exponent n in the energy-range relationship, Eq. (3), and when followed by the same normalization procedure as that described above (Section 2.2), the different RYC corresponding to different k values are independent from material parameters such as A and E_{se} in Eq. (5) but also ρ and C in Eq. (3) and they may be easily calculated with a desk-top computer. With the most frequently choice for

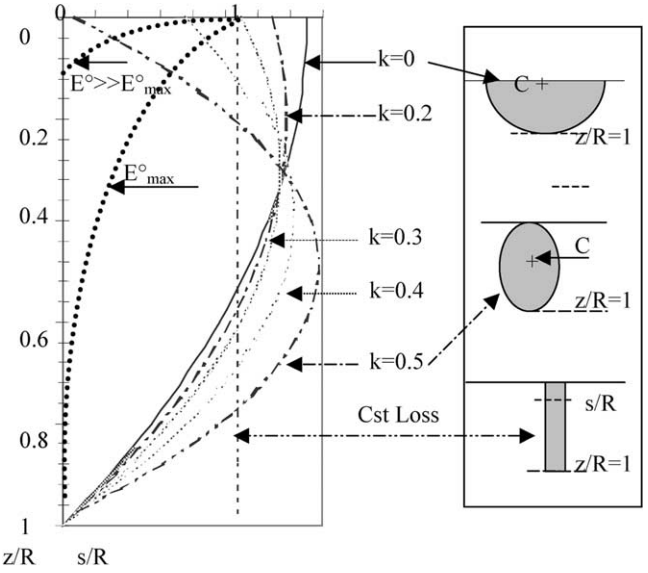

Fig. 3. Sketch of the in-depth SE generation calculated from present model, Eq. (4), compared to that of standard model (for the same total number of generated SEs, n_{se}). Symbols: experimental results [40]. Dashed lines: exponential attenuation function, for $E^0 \gg E^0_{max}$ (or $R \gg s$) and $E^0 \sim E^0_{max}$ (or $R \sim s$). Right inset: sketch of the irradiated volume postulated in present model (for $k \sim 0.1$ and $k \sim 0.5$) compared to that postulated in standard model, Cst loss (bottom right).

exponent n, $n = 1.35$, examples of such calculations are given, dotted lines, in Fig. 1(a) for KBr where the best k value is $k \sim 1/3$ and in Fig. 1(b) for MgO and Al_2O_3 where the best k value is $0.475 < k < 0.45$. Fig. 2 shows calculated RYC for k ranging from $k = 0$ to $k = 0.5$ and it illustrates the decrease of k with the increase of $\langle Z \rangle$ with, for instance, $k \sim 0.475$ for BeO and $k \sim 0$ for Pt.

The influence of k on normal yield curves is maximum when E^0 is at around E^0_{max} (or when R is of the order of 1–3 s) because, at a given depth z, the attenuation factor acts on a fraction of generated SE, dn_{se}, dramatically dependent upon the k value (see Fig. 5 in [38]) but the in-depth distribution shown in Fig. 3 when weighted by the exponential attenuation function (dashed lines) does not permits to show this influence in the presented RYCs because of the normalization to unity at this maximum. The influence of k on the RYCs is more clear in Fig. 3 when E^0/E^0_{max} is $\gg A$ (i.e., for $R \gg s$). In this situation, only the fraction of SE generated at the surface may escape into the vacuum and this surface fraction increases when k decreases and this increase more rapid when k varies from 0.5 to 0.4 than when k varies from 0.2 to 0. This remark explains the significant difference between RYCs of different light materials, k changing from 0.5 to 0.4, and the specific field of application of present model to polymers and other very low $\langle Z\rangle$ materials [38,39].

For predicting the RYC of a new compound of known $\langle Z\rangle$ value, the remaining problem is the choice of the best value for parameter k, keeping in mind that the influence of k on RYC only concerns the large E^0/E^0_{max} values. One possibility is to use the compilation of the experimental k values shown in Fig. 4, where are reported the k values deduced from present investigation (Figs. 1 and 2) combined to that recently obtained for polymers [38], for graphite and for some aromatic compounds [39] with, in addition, the k values deduced from published data obtained on Nb, $Z = 41$, and Pd, $Z = 46$ [41]. It is then possible to interpolate the experimental results or to select the experimental k value of a compound having nearly the same $\langle Z\rangle$ value: for various mica or silica glasses, for instance, a good choice is the k value of Al_2O_3 or that of SiO_2: $k \sim 0.425$–0.45. An alternative possibility is to use a pure empirical expression of the form: $k \sim 0.5 - (\langle Z\rangle/200)$, or to use Eq. (6), inspired by Kanaya and Ono [42] and reported by Niedrig [37]:

$$k = z_C/R = 0.5e^{-0.022\langle Z\rangle}. \quad (6)$$

Except the trends, decrease of k when $\langle Z\rangle$ increases, the agreement between calculated (Eq. (6)) and experimental k values is rather poor because the unknown confidence degree in Eq. (6) and the rather large uncertainties in the experimental evaluation of k (see discussion at the end of Section 2.1), or the imperfections of the present model. The development of modern data acquisition systems permits to expect better experimental estimates in the future mainly for light materials where a slight change of k from 0. 475 into 0.4 may lead to deviations increasing with E^0/E^0_{max}. Finally, improved models may be imagined to better describe the shape of the SE in-depth generation but any improvement would be paid by mathematical complications and it not sure that the final result would be more useful for practical purposes.

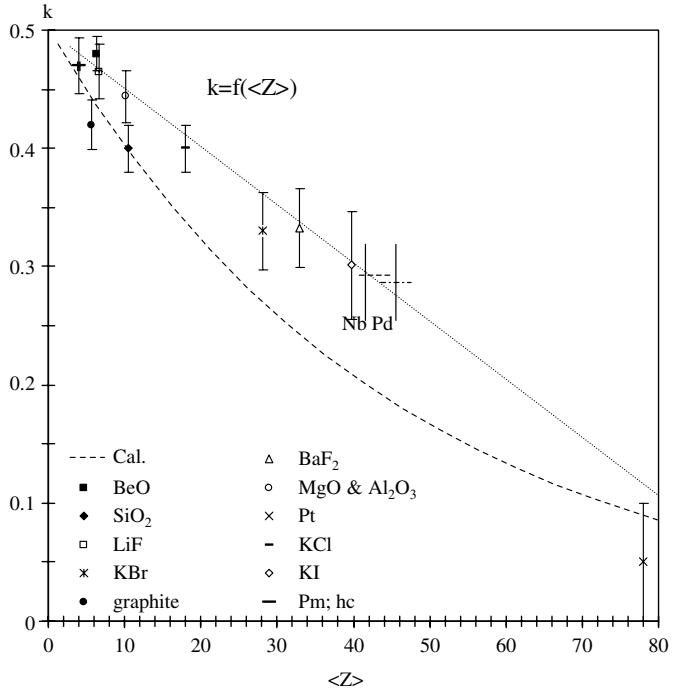

Fig. 4. Evolution of parameter $k = z_C/R$ as a function of $\langle Z\rangle$. Dashed line: calculated from Eq. (6). Faint line: empirical expression, $k \sim 0.5 - (\langle Z\rangle/200)$. Symbols: values deduced from the fitting procedure of Figs. 1 and 2; from [38] for polymers (pm) and from [39] for graphite and for some hydrocarbons (hc).

3.2. Selected applications

3.2.1. Normal yield curves, $\delta = f(E^0)$: extrapolation and critical energy, E^0_2

The best test of present model is a direct comparison between the initial experimental results and the NYC, $\delta = f(E^0)$ calculated from Eq. (5). Such a comparison is illustrated in Fig. 5, where the calculated NYC are deduced from the RYC by multiplying the reduced energy scale by the experimental value E^0_{max} and by multiplying the reduced yield by the experimental value δ_{max}. Fig. 5(a) shows the agreement between calculated NYC with $k = 1/3$ and four series of experimental results (symbols) obtained on KBr [16,17]. Also excellent, Fig. 5(b), is the agreement between calculations with $k = 0.45$ and four series of experimental results obtained on MgO [18–20] and on Al_2O_3 [21]. Finally, calculations with $k = 0.475$ fit very well the experimental results of two types of BeO specimens [22]: Fig. 5(c). A consequence of these agreements is that the full evolution of total yield curve of a given sample may be given in the form of an analytical expression, Eq. (5), from only the values at maximum, E^0_{max} and δ_{max}, with the k value of a material of same (or similar) $\langle Z\rangle$ value.

When, for technical reasons, the available experimental data is limited up to $E^0 \sim 3$–5 keV, the extrapolation of the calculated SEE yield above the investigated energy range is possible within the limits of application of the energy-range relationship, Eq. (3). This application is illustrated in Fig. 5(b) and (c), where the extrapolation up to twice this

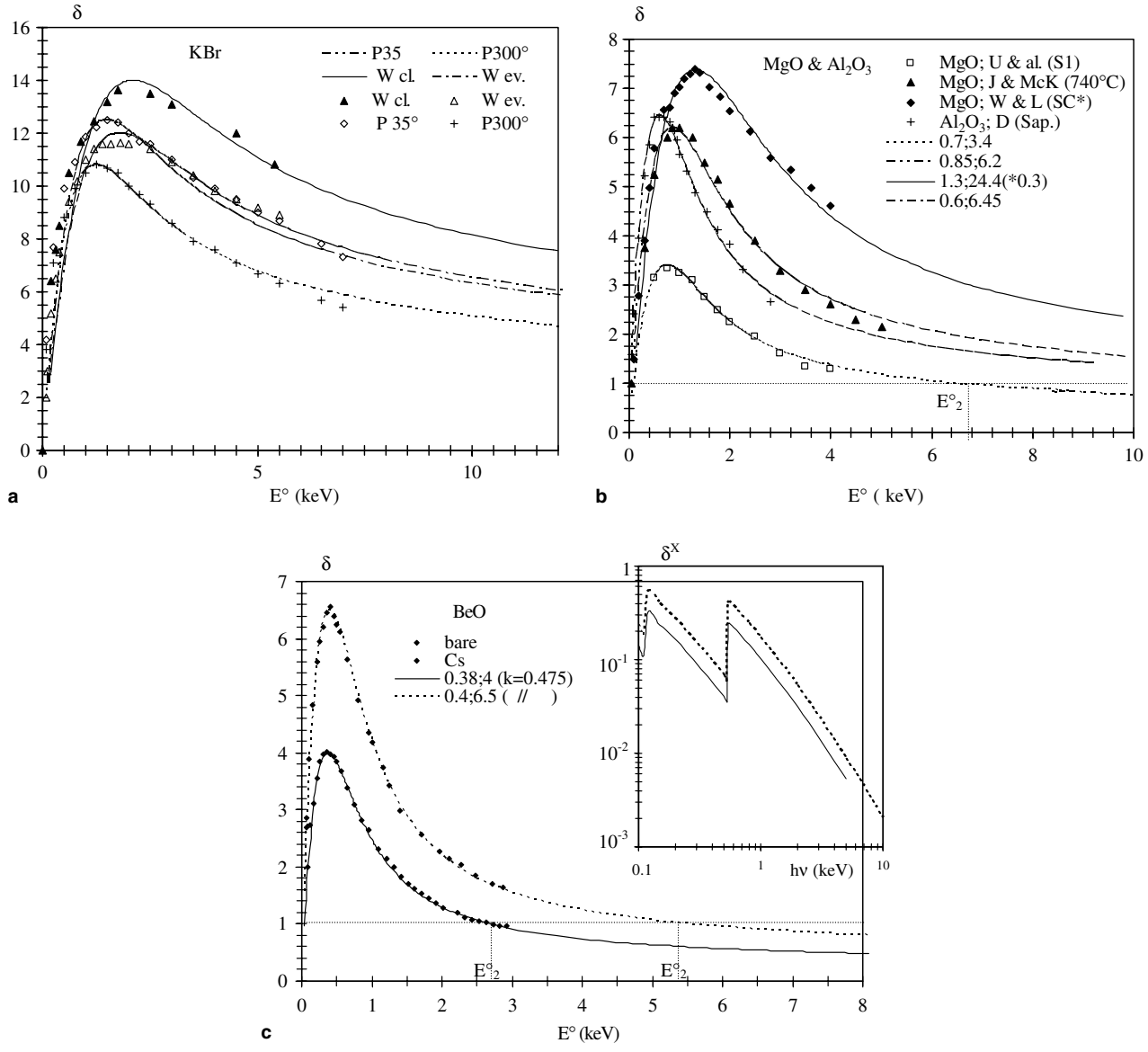

Fig. 5. Comparison between experimental normal yield results (symbols) and curves $\delta = f(E^0)$ calculated from Eq. (5). (a) KBr (same symbols as in Fig. 1(a)) and $k = 1/3$. (b) MgO and Al_2O_3 (same symbols and legends as in Fig. 1(b) plus results obtained on as-received sapphire [21]) and $k = 0.45$. Experimental and calculated yields, δ, for a MgO single crystal (SC*) [18] have been multiplied (*) by 0.3. The experimental values of E^0_{max} (in keV) and δ_{max} are indicated in legend. (c) BeO with symbols related to bare surface (bare) and to caesiated surfaces (Cs) [22] and lines calculated with $k = 0.475$. In inset: log–log scale of the X-ray-induced secondary electron emission from BeO, $\delta^X(h\nu)$ calculated from Eq. (9), with parameter' values deduced from present δ experimental results. In (b) and (c), the extrapolation procedure permits to estimate E^0_2.

largest energy seems reasonable. The same extrapolation procedure also permits to estimate the critical energy E^0_2, where the yield is equals to the unity. For specimens having δ_{max} values of a few unities or less, E^0_2 is directly obtained from a graphical construction similar to that shown in Fig. 5(b) and (c), where E^0_2 is ~6.6 keV for a polycrystalline variety of MgO, and it is ~2.7 and ~5.4 keV for the two varieties of BeO. For specimens having larger δ_{max} values, E^0_2 may be estimated from the asymptotic form of Eq. (5) (Eq. A6 in [38]) with parameters' values, A/E_{se} and s, deduced from the normalization procedure.

For the insulators of interest, the estimated values of E^0_2 are summarized in Table 1 with an increasing uncertainty with E^0 because the inherent uncertainty of any extrapolation procedure and the uncertainty on the validity of exponent $n = 1.35$ in Eq. (3) for PE energies larger than 10 keV. One also may point out that energy E^0_2 increases with δ_{max} and like it, it depends upon the crystalline state, temperature, surface state, etc., specific to each investigated specimen and not characteristic of a given insulator only defined by its chemical composition.

3.2.2. Deduced values for s and A/E_{se}

From the weighting factors, R_{max}/s and p, used to set E^0/E^0_{max} and δ/δ_{max} equals to the unity (Sections 2.2 and

Table 1
Experimental and calculated values of parameters for the insulators of interest

	E^0_{max} (keV)	δ_{max}	k (R_{max}/s; p)	S (nm)	A/E_{se} (keV^{-1})	E^0_2 (keV)	E^C_2 cal (keV)	E^C_2exp (keV)
LiF [17] cl	0.6	7.2	0.475 (2.0; 2.1)	12.5	25.2	~10	0.8	
KCl [17] cl	1.25	13.2	1/3 (2.7; 2.5)	26.6	26.4	>30	1.35	1.7 [55]
KI [17] cl	1.5	10.4	0.3 (2.8; 2.53)	22.8	17.3	>30	1.6	
BaF2 [17]	0.8	6.0	~1/3 (2.7; 2.5)	6.5	18.8	>25	0.9	1.6 [55] CaF_2
KBr			1/3 (2.7; 2.5)					
[17] cl.–ev.	2.1–1.8	14–12		42–34	18; 18	>30; >30	2.3–1.9	
[16] 35–100°	1.5–1.42	12.5–11.7		27–25	22.5; 22	>30; >30	1.6–1.5	
[16] 200–300°	1.3–1.25	11.2–10.8		22–20.9	23; 23.3	>30; >30	1.4–1.35	
BeO [22] b–cs	0.38–0.4	4–6.5	0.475 (2.0; 2.1)	5.1–5.5	22; 34	2.7; 5.4	0.5	
SiO_2 [24] w	0.4	4.05	0.425 (2.25; 2.4)	6.45	24.3	7 ± 2	0.5	1 [60]
Al_2O_3			0.45 (2.1; 2.0)					2 [58,59]
ar-hp Sap [21]	0.6–0.6	6.45–7.85		7.9–7.0	23–30	20–>30		
MgO			0.45 (2.1; 2.0)					1.5–2.5 [57]
RT: 740° [20]	0.95; 0.85	7.15–6.3		14–12.	17.3–17	>30; 30	1.2–1.1	
sc: tf [18]	1.3–1.1	24.6–19.5		21.4–16.1	~43–41	≫30; >30	1.7–1.4	
S1–S2 [19]	0.75; 1.1	3.4–3.6		10.2–17	10.4–7.5	6.5; 10.5	1–1.4	

E^0_2 values: estimated from extrapolation of experimental results; E^C_2 cal values: calculated from $R \sim 3s$. E^C_2 exp[]: critical energy obtained in independent measurements on different specimens but with the chemical symbols indicated in the corresponding line. Symbols. cl: cleaved; ev: evaporated; b: bare; cs: caesiated; w: wet; ar: as-received; hp: highly polished; sc: single crystal; tf: thin film.

3.2.1), it is possible to obtain useful numerical values for the SE attenuation length 's', and for A/E_{se} of the investigated specimens [38]. Using standard model with $n = 1.4$, a similar procedure has been applied to a variety of insulators and semiconductors by Grais and Bastawros [5] but the use, here, of a better model permits to expect better values. Table 1 summarizes the selected experimental values for E^0_{max}; δ_{max}; k; R_{max}/s and p followed by the calculated values of s (from Eq. (3) with $n = 1.35$ and $C = 115/\rho$) and of A/E_{se}. From Table 1, it is seen that the SE attenuation length, s, varies from ~5 nm up to 42 nm with a mean value larger than that of metals: 0.5–1.5 nm [3] and also larger than that deduced from standard model: 3.9 nm for LiF; 13.6 nm for KCl; 14.6 nm for KI; 5.1 nm for KBr [5]. The influence of the crystalline state is clearly seen with 's' starting from $s \sim 5$–7 nm for the amorphous forms of SiO_2 and BeO up to $s \sim 42$ nm for a KBr single crystal. In between, there is the increase of 's' when going from evaporated alkali halides to cleaved single crystals such as KBr or the increase of 's' with the crystallite size for MgO specimens from thin disordered films to single crystal [18,19]. Similarly to the increase of crystalline disorder, the increase of temperature leads to a decrease of 's' via now the increase the SE interaction with atomic vibrations: 's' decreases from ~27 nm at room temperature down to ~21 nm at 300 °C for KBr crystals [16] and from 14 nm at room temperature to 12 nm at 740 °C for MgO crystals [21].

As a consequence of the change of SE escape probability, A, the estimated value of A/E_{se} is larger for a ceasiated BeO surface than for a bare BeO surface [22] and larger for highly polished sapphire than for 'as received' sapphire [20]. The insensitivity to temperature (within the experimental uncertainties) for KBr and MgO has also to be pointed out.

3.2.3. Estimate and discussion of the escape probability, A, from insulators

The escape probability A may be estimated from the A/E_{se} values of Table 1 when E_{se} is known. For the wet SiO_2 sample [24], one obtains $A \sim 38\%$ for $E_{se} \sim 16$ eV [43] ($\chi = 0.9$ eV; band gap energy: $E_G \sim 9$ eV) and $A \sim$ 35–45% for the two types of sapphire (as-received and highly polished Al_2O_3) [21]. For the other wide band gap insulators of interest, precise E_{se} values are missing but they nearly correspond to $E_{se} \sim 2E_G$ instead of $E_{se} \sim 3E_G$ for semiconductors [43–45]. From compiled values of E_G [5,46], one obtains $25\% < A < 50\%$ except for the MgO single crystal investigated by Whetten and Laponsky [18] for which A is founded to exceed 60%.

To discuss these values, direct calculations of A may be performed from the SE transmission probability across the surface potential barrier, $T(S/V)$ [11,12]:

$$T(S/V) = \frac{4G^{1/2}}{[1+G^{1/2}]^2} \text{ with } G = 1 + \frac{E_S - E_k}{E_k \cos^2\gamma}, \quad (7)$$

where E_k is the SE kinetic energy in the vacuum and E_S is the corresponding kinetic energy in the specimen; then $E_S = E_k + \chi$ for insulators (and semiconductors) of electron affinity χ [46]. The angle of emission into the vacuum γ is related to the inner angle of incidence, β, by a refraction law of the form [46]:

$$\sqrt{E_S}\sin\beta = \sqrt{E_k}\sin\gamma. \quad (8)$$

For $E_k = 0.5$; 1; 2 eV and $\chi = 0.5$; 1; 1.5 eV, the calculated transmission probability as a function of the inner angle, $T(\beta)$, top of Fig. 6, shows a stepped evolution with a plateaus for SE near normal to the surface where the influence of χ on $T(\beta = 0°)$ is low, $85\% < T(\beta = 0°) < 98\%$. This plateaus is followed by an abrupt fall near from the critical angle for total internal reflection, β_l, where β_l is strongly

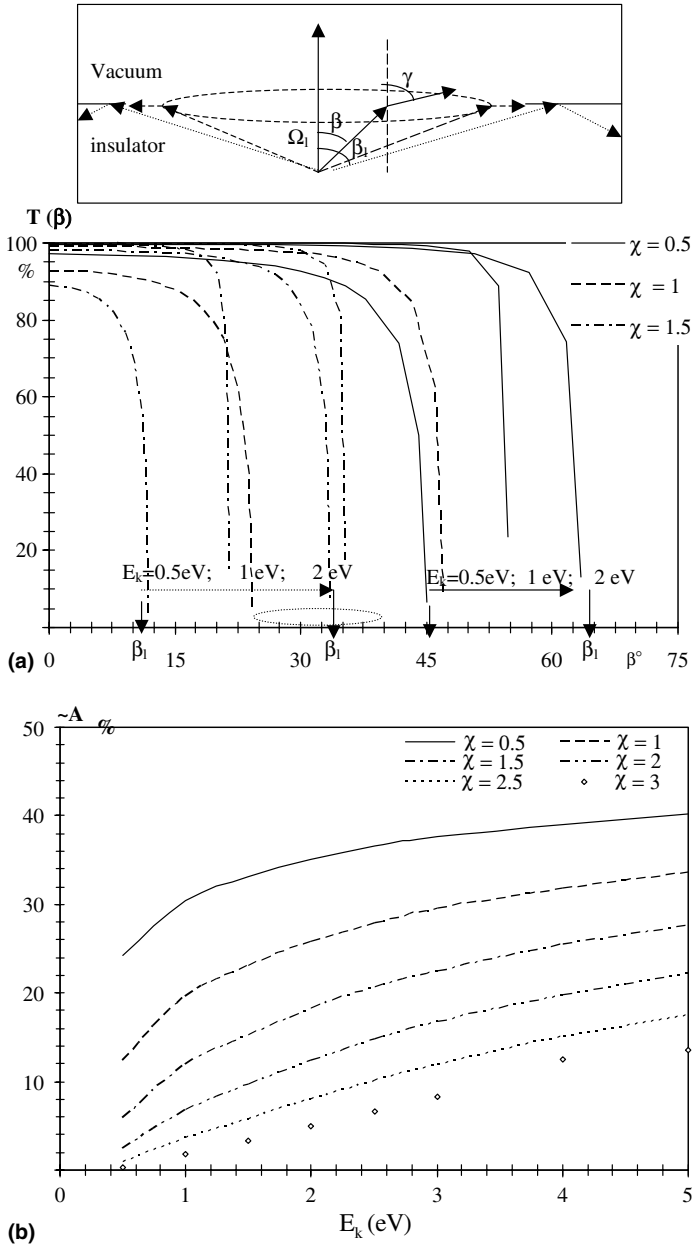

Fig. 6. (a) Calculated (Eqs. (7) and (8)) angular transmission probability, $T(\beta)$, as a function of the inner angle, β, for different SE kinetic energy into the vacuum, E_k, and material affinities, χ (in eV). (b) From $A \sim (1/2)[T(\beta = 0°)]\,(1 - \cos\beta_l)$, calculated probability, A, as a function of their most probable kinetic energy into the vacuum, E_k, for different affinities, χ. Top inset: SE refraction effect at the vacuum/insulator interface and inner total reflection.

dependent of χ: $(\sin\beta_l) = [E_k/(E_k + \chi)]^{1/2}$. Then, instead of complicated angular integrations, the escape probability may be approximated by $A \sim (1/2)T(\beta = 0°) \times (1 - \cos\beta_l)$ – see top inset of Fig. 6. When E_k is next identified to the most probable SE energy into the vacuum, the present estimate of the escape probability A is $A \sim 20$–30%, bottom of Fig. 6, for the insulators of interest when χ ranges from 0.5 eV up to 1 eV and when the most probable SE energy into the vacuum also ranges from 0.2 eV, CsI, to 1 eV, KCl, for most alkali halides, except LiF (2 eV) [46].

Compared to the A values deduced from A/E_{se}, present evaluation falls within a rather good order of magnitude, a few 10%, but A is underestimated by a factor one-half and it is limited up to 50% for $\chi = 0$ eV. Then present evaluation cannot explains the value, $A > 60\%$, obtained for some MgO crystals as well as the value of $A \sim 70$–100% for materials of zero affinity [45,47–50]. The reason is that the present estimate, based on an effective solid angle Ω_l normalized to 4π sterad, postulates a straight propagation of SE into the solids. In reality, a generated SE follows a random path and it may escape into the vacuum even when its path is initially directed towards the bulk, this at least when its transport mean free path, λ, is far less than the attenuation length, s [47–49]. Consequently, an improved estimate for $A \sim T(\beta = 0°) \times (1 - \cos\beta_l)$. Better than calculations restricted to one (z-) dimension and in good

agreement with values deduced from experiments, such an expression takes into account the SE random walk and the influence of χ on A at oblique inner incidence.

In conclusion for the two last subsections, the possibility to extract useful physical information such as the A and s values from normal yield data of the investigated specimens has been illustrated but the diversity of A and s values obtained on an insulator only defined by its chemical composition explains the diversity of the experimental $\delta = f(E^0)$ curves being acquired. These NYCs are strongly dependent upon the A and s values that vary from one specimen to another making, for instance, the SE transport sensitive to the concentration of dislocations, impurities, vacancies as well as by the crystallite dimensions and temperature of the specific specimen being investigated. This evidence makes difficult to predict easily the experimental NYC, $\delta = f(E^0)$ of most of the investigated specimens and sophisticated calculations are needed to only solve the problem of SE transport in ideal single crystals [47].

3.3. X-ray-induced secondary electron emission: $\delta^X(h\nu)$

An expression for the X-ray-induced secondary electron yield, δ^X, may be obtained in a manner similar to that used in standard model for electron-induced SEE. The mechanism involved in the generation of the (X-ray-induced) secondary electrons results from the absorption of X-ray photons, photoelectric effect, followed by the creation of energetic photo and Auger electrons generating a large number low energy SE in their slowing down in a manner similar to energetic incident electrons do. This generation is followed by the SE transport and escape that are independent from the nature of the projectile and then they may be described by parameters s and A identical to that used in present model. Then $\delta^X(h\nu)$ takes the form [29]:

$$\delta^X = [A \cdot h\nu/E_{se}]\ (\mu s) \tag{9}$$

with μ = linear X-ray absorption coefficient and $\mu^{-1} \gg s$.

For a given specimen, it is then possible to deduce the evolution of $\delta^X(h\nu)$, Eq. (9), from δ experimental results and vice versa. Using the standard model, this strategy has been applied to predict the SEE yield, δ, of solid xenon from X-ray experiments, δ^X [29], and next to verify these predictions [50]. In the context of present article, the use of A/E_{se} and s values deduced from present model permits to expect more precise results for δ^X. As an illustration, the inset of Fig. 5 shows the evolution of $\delta^X(h\nu)$ for the two varieties, bare and ceasiated surfaces, of BeO samples calculated from the present values of A/E_{se} and s and from tabulated values of absorption coefficient, μ [51].

4. Charging

4.1. General considerations

In insulators, mechanisms of charging result from a competition between negative charges injected by the incident electron beam, intensity I^0, and the positive charges left by the SEE into the vacuum combined to electrons escaping from the specimen via backscattering, and evacuation currents: respect. $\eta^C I^0$ and I_{ev}. The total charge into the specimen, Q, induces, among other, a surface potential, V_S, which directly or indirectly influences the secondary electron emission yield, δ^C (superscript ^{C} for charging with respect to the nominal SEE yield, δ and to the nominal backscattering coefficient η) modifying, in turn, the time change of Q into the specimen, $\partial Q/\partial t$ and next δ^C. The evolution of the SEE yield during irradiation is the main subject of present section where the surface potential plays a leading role.

The surface potential is a function of the charge distribution and the boundary conditions and when a flat homogeneous specimen irradiated with a widely defocused incident beam is considered, V_S is a constant over the irradiated surface. With respect to the specimen holder set to ground, it is approximately related to Q by [52]:

$$V_S(1+a) - aV_C \sim [Qh/\varepsilon S] + (\text{r.t.}) \tag{10}$$

with h is the specimen thickness; ε is the specimen dielectric constant; ε_0 is the vacuum dielectric constant (8.85×10^{-12} F/m); $\varepsilon_r = \varepsilon/\varepsilon_0$; S is the irradiated area; parameter 'a' $\sim h/\varepsilon_r w$ and w is the distance of the SE collector from the specimen surface; V_C is the bias of the SE collector (or extractor). Term (r.t.) is a residual term depending upon the in-depth charge distribution that is composed of two layers with $Q = Q_+ + Q_-$, where the positive layer, of charge Q_+ and of maximum thickness $r = 3s$, results from the positive charges left by the SEE and where the negative layer, of charge Q_- and of maximum thickness R (range of incident electrons), results from a part of incident electrons injected into the specimen. More precisely this residual term is nearly given by (r.t.) $\sim [Q_+ r + Q_- R]/2\varepsilon S$ for a rectangular in-depth charge distributions and it is often negligible except when $Q_+ + Q_- \sim 0$. In many geometries, parameter 'a' is also negligible and Eq. (10) simplifies to the classical relationship of a plane capacitor, $Q = CV_S$ with $C = \varepsilon S/h$.

Numerical application of Eq. (10) shows that surface potential of +1 V is obtained with an excess of positive charge density, $Q/S = (Q_+ + Q_-)/S$, of only $+3 \times 10^{-8}$ C/m^2 or <0.2 hole/μm^2 for $h = 1$ mm and $\varepsilon_r = \varepsilon/\varepsilon_0 = 3.4$. This very low value shows that a small amount of charges in excess is sufficient to produce a significant surface potential but the weight of V_S on the SEE yield depends upon the nominal energy of the primary electrons E^0. Various regimes may be then considered with a special attention to energy, E_2^C, where the range of incident electrons R is nearly equals to the maximum escape depth of the SE, because the generated SE and holes being localized in the region, may recombine easily each others when $E^0 < E_2^C$. The calculated values of E_2^C for the insulators of interest are shown in Table 1 with $R \sim r \sim 3s$ [because exp-(3) ~5% for an exponential SE attenuation] and it may be seen that the E_2^C values are slightly larger than E^0_{max} and often far less than E_2^0.

4.2. Influence of V_S on the SEE yield for different beam energies E^0

4.2.1. $E_1^0 < E^0 < E_2^C$

For $E_1^0 < E^0 < E_2^C$, more SE electrons initially escape into the vacuum than PE penetrate into the target, $(\delta + \eta) > 1$, and the positive charges in excess are distributed inside a surface layer of thickness $d_+ \sim R < 3s$. At the early beginning of the irradiation, V_S becomes positive and the generated SE having a kinetic energy normal to the surface, $E_{K\perp} = E_K \cos^2\gamma$, less than $-qV_S$ ($-q = 1.6 \times 10^{-19}$ C) into the vacuum are reflected back to the surface when the bias of a plane collector, V_C, is $V_C < V_S$ and the reflection effect strongly increases with γ (see top inset of Fig. 7). Even for a hemispherical collector or hemispherical constant-potential surfaces into the vacuum and a collector set at ground, the main effect of a few volts surface potential is the rapid decrease of $\delta^C + \eta^C$ down to the unity because of the low value of the most probable energy of SEs emitted from insulators: see band structure scheme in the top of Fig. 7. When the external collector is positively biased, $V_C > 0$ (see bottom of Fig. 7), the decrease of $\delta^C + \eta^C$ down to the unity is delayed until V_S reaches a few volts above the V_C value: $V_S - V_C \sim +2$–3 V.

Additional effects may happen such as, bottom of Fig. 7, the possible SE extra-emission due to the band bending in the charged region when the detector is biased [50]. In this region, the potential function, $V(z)$, is more or less parabolic and the potential difference, $\Delta V = V_S - V(d_+)$, between its value at surface and its value at $z \sim d_+$, may increase the SEE yield. The relative difference is of about $\Delta V/V_S \sim d_+/h$ and ΔV may reach a fraction of volt for thin layers of highly secondary electron emitters such as condensed rare gases, Ne, Ar, Kr, Xe, where the attenuation length (and the d_+ distance) may reach a few tenths of micron [45,50]. There are also electric field effects. The electric field in the vacuum is the sum of the electric field induced by the positive charges in the specimen, F_C and the applied electric field associated to the bias of the collector. These two fields are of opposite direction in the vacuum but they add their effect in the specimen (see open arrows in Fig. 7). The mean value of the field in the specimen is $\sim V_S/h$ and it may reach significant values only when the bias of the detector, V_C, is very large. Except in specific situations, the risk of leakage at $z \sim r$ is low.

4.2.2. $E_2^C < E^0 < E_2^0$

For $E_2^C < E^0 < E_2^0$, more SE electrons initially escape into the vacuum than PE penetrate into the target, $(\delta + \eta) > 1$. At the early beginning of the irradiation, the surface potential starts again to be positive. But the charge distribution evolves because of the decrease in number

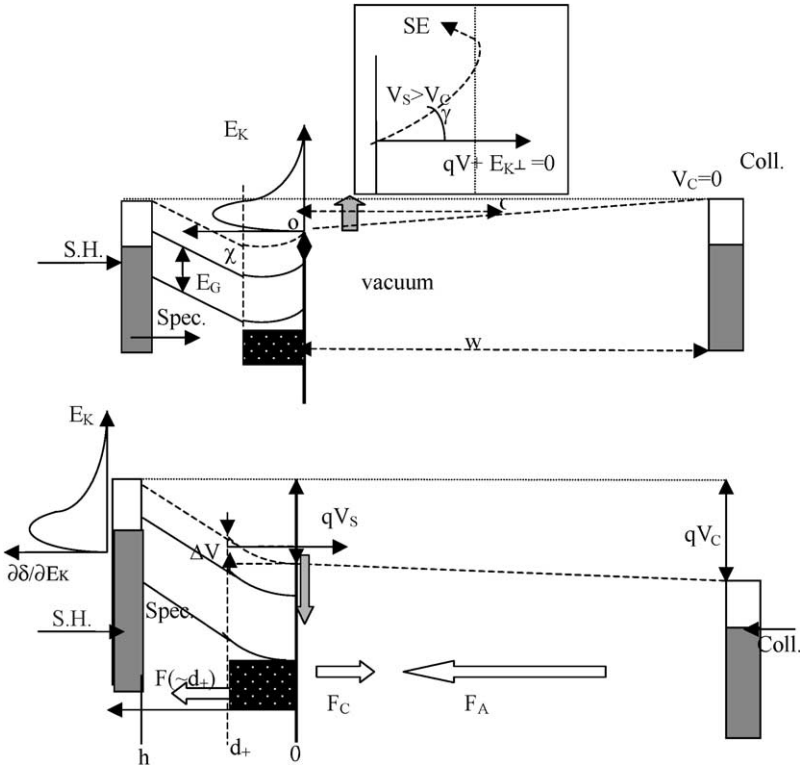

Fig. 7. Band structure scheme of a positively charged insulator, $V_S > 0$, when the collector is set at ground (top) and when it is positively biased: $V_C > V_S$ (bottom). Top inset: reflection effect of some low energy SEs (mainly those emitted at oblique emergence) for $V_C > V_S$. Open horizontal arrows: directions of the fields; grey vertical arrows: trends for q V_S. The initial (non-charged) spectral distribution of the emitted SE, $\partial\delta/\partial E_k$ is also shown. S.H.: specimen holder (at ground); coll.: collector; Spec.: specimen.

of newly generated holes at surface and the constant accumulation of electrons deeper in the bulk. Then V_S has to change sign for permitting the recombination of new arriving electrons with new generated holes. For instance when E^0 is chosen to be $E^0 = E_2^0$, the initial number of incoming electrons is equals to the initial number of emitted electrons, $|Q_-| = Q_+$, but the positive charges are located at the surface and negative charges are located deeper in the bulk so the electrostatic system corresponds to a dipolar layer that induces non-null electric fields and potential in all the space except in a mid-plane between the two layers of opposite sign: $V = 0$ at depth $z = r$ (see top of Fig. 8). At surface $z = 0$, V_S is governed by the residual term, (r.t.) of Eq. (10) and it is slightly positive, reducing then a part of the SEE to the benefit of new incoming electrons and $\partial|Q_-|/\partial t$ starts to be larger than $\partial Q_+/\partial t$. From positive the surface potential rapidly becomes negative because of the increasing incoming of negative charges. The steady state occurs when the surface potential change is stopped, $\partial V_S/\partial t = 0$: a condition only satisfied when the effective PE range, R^C, is nearly equals to the maximum SE escape depth: $R^C \sim r$ (or $\sim 3s$) and also corresponding to a

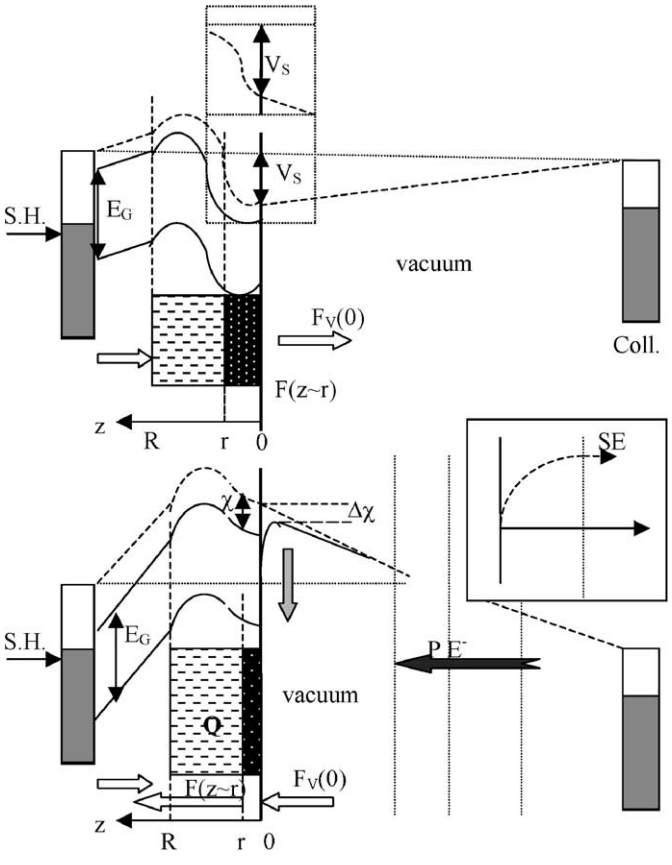

Fig. 8. Band structure scheme for $E^0 = E_2^0$ (top) and for $E^0 > E_2^0$ (bottom). In the top, the in-depth potential function, $V(z)$, is that of the dipolar layer ($Q_+ = -Q_-$) with $V(z \sim r) = 0$ and $V_S = V(0) > 0$. The bias of the collector is $V_C = 0$ and it is $V_C > V_S$ in the top inset. For $E^0 > E_2^0$ (bottom) the main external effect is the slowing down of PE: full horizontal arrow. Also shown: Schottky barrier lowering, $\Delta\chi$; distortion of the SE trajectories (inset) and internal field maximum at $z \sim r$.

time change of $Q_+r + Q_-R$ equals to zero. Then when E^0 is in interval $E_2^C - E_2^0$, the critical energy E_2^C attained at the steady state is less than E_2^0 and a negative surface potential is established to decrease the penetration depth of the new arriving incident electrons via their external slowing down. With $q = -1.6 \times 10^{-19}$ C, V_S is given by [52]:

$$qV_S = E^0 - E_2^C. \tag{11}$$

The key point of present approach is that the steady implies not only $\delta^C + \eta^C = 1$ but also $R^C \sim r$ for a rapid recombination between new injected PE and new generated holes. When the collector is positively biased the scenario remains the same but slightly delayed in time.

4.2.3. $E^0 > E_2^0$

For $E^0 > E_2^0$, less SE electrons escape into the vacuum than PE penetrate into the target because $(\delta + \eta) < 1$ and the surface potential starts to be negative. The main effect of a negative surface potential is the external slowing down of the PE arriving at the surface with an effective kinetic energy $E = E^0 - qV_S$ (with q and $V_S < 0$) and this slowing down increases the SEE yield. The electro-kinetic situation evolves towards the balance $\delta^C + \eta^C = 1$ when the evacuation current, I_{ev}, is negligible and the steady state again corresponds to $\partial V_S/\partial t = 0$, that is attained when new injected PE and new holes left by the SEE may recombine easily that is to say when $R \sim 3s$. The effective landing energy is the critical energy E_2^C. Consequently, V_S is again given by Eq. (11) and correlated to the increase of $|Q_-|$, $|V_S|$ increases with E^0. With respect to situation of Section 4.2.2, the main quantitative difference is the large absolute value taken by V_S: $|V_S| \sim 18$ kV for experimental E_2^C value of around ~ 2 keV when a high PE energy $E^0 \sim 20$ keV is chosen.

Such large potential values induce additional electric field effects (see the band structure scheme in the bottom of Fig. 8). The large electric field strength into the vacuum side, F_V, may lead to a lowering of the effective affinity, $\Delta\chi$ [52] with $\Delta\chi = q\sqrt{qKF_V/\varepsilon_0}$ and $K = (\varepsilon_r - 1)/(\varepsilon_r + 1)$. When $|V_S|$ is ~ 18 kV, the field strength is $\sim 1.8 \times 10^6$ V/m for a vacuum gap width, w, of ~ 1 cm and $\Delta\chi$ is ~ 0.18 eV for ε_r is ~ 3.4 and a slight extra SE emission is possible. Another external field effect is the longitudinal acceleration of the emitted SE leading to vacuum trajectories rapidly parallel to the normal to the surface with the risk for the collected energetic SE to generate in turn a SEE emission from the collector material. In the specimen, the mean field strength is given by V_S/h and it is one order of magnitude larger than F_V when the specimen thickness is $h \sim 1$ mm. But the internal field is not uniform, it is maximum in the plane $z \sim r$, where the positive and the negative charges add their effects. The risk of an electric breakdown is high at $z \sim r$ where a depletion zone takes place. Inside the specimen but outside the irradiated volume, the field direction drives towards the grounded specimen holder the electrons generated near from $z \sim R$.

4.2.4. Synthesis of the evolution of δ^C with E^0

Inspired from [52], Fig. 9 summarizes the above discussion by showing the expected evolution of the SEE yield for different initial beam energies $E_A^0(E_1^0 < E_A^0 < E_2^C)$; $E_B^0(E_2^C < E_B^0 < E_2^0)$; $E_D^0(E_D^0 > E_2^0)$ when the evacuation current, I_{ev}, is negligible. Through qV_S given by Eq. (11), the horizontal arrows represent the surface potential V_S attained at the steady state. The charge conservation relationship permits also to show that the excess of charges, Q, accumulated during irradiation is nearly proportional to the hatched area shown in the same figure. When applied to a closed surface surrounding the irradiated volume (dotted line in inset of Fig. 9), the charge conservation may be written in the form [52]:

$$I^0 = I^0(\delta^C + \eta^C) + \partial Q/\partial t + I_{ev}. \tag{12}$$

When the evacuation current I_{ev} is negligible, the integration of Eq. (12) from the initial time up to the steady state leads to:

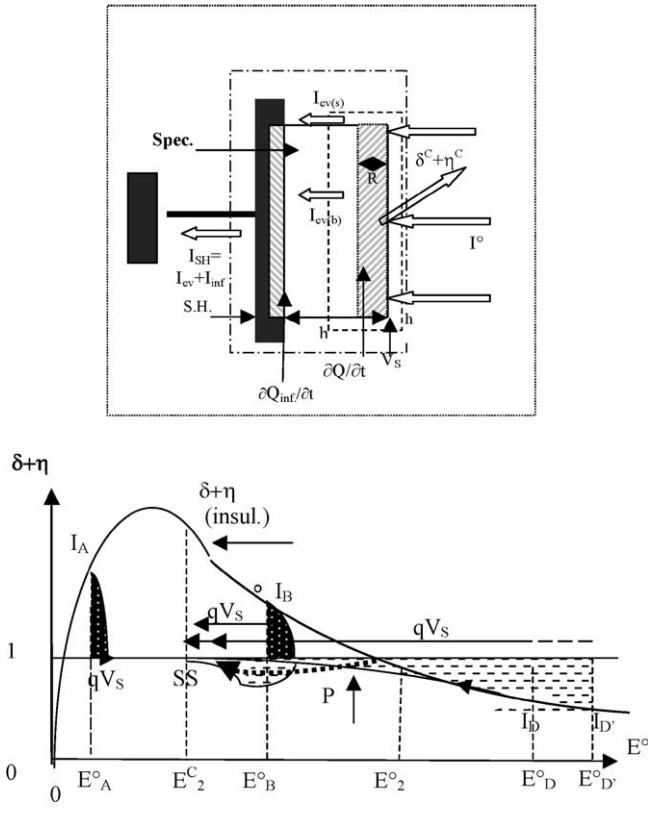

Fig. 9. Expected evolution of $\delta + \eta$ from the initial energy E^0 to the steady state for different initial energies, E^0. Hatched areas are proportional to the charge Q into the specimen with $Q > 0$ above the horizontal line $\delta + \eta = 1$ and $Q < 0$ below it. When E^0 is $E^0 > E_2^0$, its increase from the initial point I_D to $I_{D'}$ leads to the simultaneous increase of $|V_S|$ and of $|Q|$. Dotted line from E_2^0 to E_2^C corresponds to an initial energy $E^0 \sim E_2^0$ (see also the top of Fig. 8). Top inset. Charge conservation relationship applied to a volume limited by the dashed rectangle: Eq. (12). Q_{inf}: Charge of opposite sign developed by influence on the inner surface of the specimen holder that has to be taken into account when the relationship is applied to the dashed-dotted rectangle. I_{ev} ($=I_{ev(s)} + I_{ev(b)}$) is the sum of the charge evacuation by the surface and through the bulk; I_{SH}, specimen holder current.

$$Q = -I^0 \int_0^\infty [\delta^c(t) + \eta^c(t) - 1]\,dt$$
$$= -I^0 \int_0^\infty [\delta^c(E) + \eta^c(E) - 1](\partial E/\partial t)^{-1}\,dE, \tag{13}$$

where the integral of the term $[\delta^c(E) + \eta^c\ E - 1]dE$, effectively corresponds to the hatched areas with $Q > 0$ for the area above the horizontal line, $\delta^c(E) + \eta^c(E) = 1$ and $Q < 0$ for the area below this line.

For $E^0 = E_A^0$ with $E_1^0 < E_A^0 < E_2^C$, Q and V_S are both positive. For $E^0 = E_D^0$ with $E_D^0 > E_2^0$, Q and V_S are both negative. The increase of E^0 from E_D^0 to $E_{D'}^0$ leads to the simultaneous increase of $|V_S|$ and of $|Q|$ and the increase of $|Q|$ is represented by the increase of the hatched area below the horizontal line $\delta^c(E) + \eta^c(E) = 1$ of Fig. 9: an analysis consistent with the recently observed increase of Q with E^0 for quartz [53]. Finally for $E^0 = E_B^0$ with $E_2^C < E_B^0 < E_2^0$, a negative lobe for Q is required to obtain consistent signs for Q and V_S, both being finally negative at the steady state.

An alternative illustration is to show the change of $\delta^c(t) + \eta^c(t)$ as a function of the fluence, $I^0\tau/S$. For $E^0 = E_A^0$ with $E_1^0 < E_A^0 < E_2^C$, the rapid decrease of $\delta^c(+\eta^c)$, when the collector is set at ground and its delayed decrease when the collector is biased are shown in Fig. 10(a). Also shown in Fig. 10(a) is the slow increase of $\delta^c(+\eta^c)$ when $E^0 = E_D^0$ with $E_D^0 > E_2^0$. The use of plane capacitor approximation, $V_S \sim \varepsilon Q/hS$ (Section 4.1 and Eq. (11)) combined to charge conservation law, $Q/S \sim (I^0\tau/S)\ [\delta + \eta - 1]$, permits to obtain some quantitative estimate and orders of magnitude for the initial time interval, τ. For instance, one obtains $V_S \sim 1$ V for the incident charge density $I^0\tau/S$ of $\sim 3 \times 10^{-8}$ C/m^2 and $\delta + \eta \sim 2$ (positive charging), the other values being (see Section 4.1): $h = 1$ mm and $\varepsilon_r = \varepsilon/\varepsilon_0 = 3.4$. This charge density corresponds to $I^0 \sim 1$ nA into a spot area of $S = 1$ mm^2 with $\tau = 30$ μs and such a low surface potential is sufficient to reduce the SEE yield of a few 10% when the collector is set at ground (see Section 3.2.2). The decrease of the SEE yield is delayed of around 1 ms when the collector is positively biased at $V_C \sim 40$ V (the other parameters being unchanged). For the same specimen and the same fluence the decrease of V_S is less than ~ -0.5 V when E_D^0 is larger than E_2^0. Such a negative charging obtained with, saying, $\delta\ (+\eta) \sim 0.8$ cannot induce a sufficient PE slowing down for giving rise to a detectable change of the SEE yield during a 30 μs-pulse duration. A detectable change of $\delta\ (+\eta)$, saying from 0.8 to 0.9, is attained when $V_S \sim -1$ kV and it requires the increase of three orders of magnitude of the pulse duration of the incident beam density. Then for the point of view of the time evolution during irradiation, the major difference between the two situations is not only the opposite sign but also the magnitude of the change of the SEE yield with a much more rapid decrease when the surface potential is positive than its increase when the surface potential is negative.

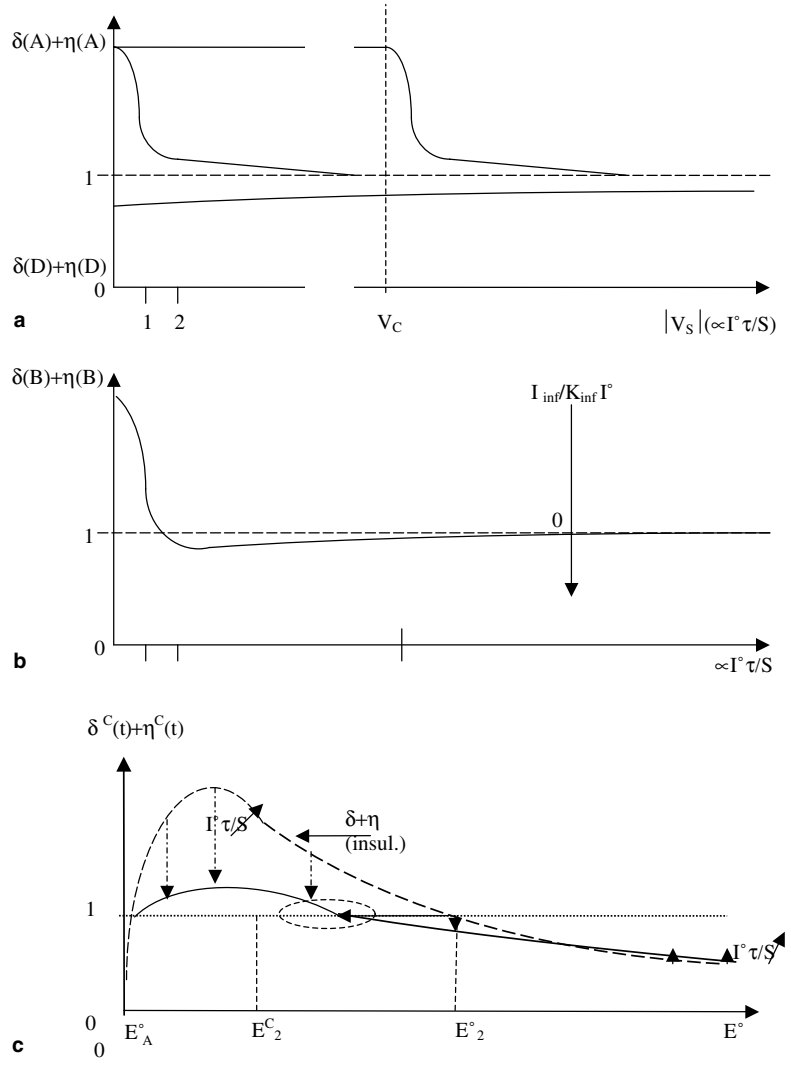

Fig. 10. Expected time evolution of $\delta + \eta$ from the initial yield to the steady state ($\delta^C + \eta^C = 1$). (a) $\delta(A) + \eta(A)$ for $E_1^0 < E_A^0 < E_2^C$ showing the ultra-rapid decrease of $\delta(A) + \eta(A)$ that is delayed when $V_C > 0$. For $E_D^0 > E_2^0$, $\delta(D) + \eta(D)$ shows a very slow increase. (b) $E_2^C < E_B^0 < E_2^0$, showing the change of sign of $\delta^c(t) + \eta^c(t) - 1$, during irradiation and the change of sign of I_{inf}, related change of $\partial Q/\partial t$. (c) Expected distortion of $\delta + \eta$ as a function of the nominal (or initial) PE energy E^0 for a given $I^0\tau/S$ value with the much more rapid decrease of $\delta + \eta$ when $E_1^0 < E^0 < E_2^0$ than its increase when $E^0 > E_2^0$ and the shift of the critical energy from E_2^0 to E_2^C with a possible break in the slope of the yield (see circled zone).

For $E^0 = E_B^0$ with $E_2^C < E_B^0 < E_2^0$, the expected time evolution of $\delta^c(t) + \eta^c(t)$ combines the rapid decrease of a positive charging and the slow increase of a negative charging. This time evolution is shown in Fig. 10(b), where the variable is now proportional to $I^0\tau/S$ and not V_S because the plane capacitor approximation does not hold. Correlated to the change of sign of $\delta^c(t) + \eta^c(t) - 1$, in Fig. 9, there is the change of sign of $\partial Q/\partial t$ leading to the correlated change of sign of the influence current I_{inf} providing a possible an explanation to the experiments reported by Paulhé et al. [54] on some ceramics.

Fig. 10(c) summarizes the full distortion of yield curve as a function of the nominal PE energy E^0 for a given $I^0\tau/S$ value. Besides the more important distortion for the energetic interval $E_1^0 < E_A^0 < E_2^C$ than for the energetic interval $E_D^0 > E_2^0$ the other point to outline is the beginning of the shift of the critical energy E_2 from E_2^0 towards E_2^C (only attained at the steady state) with a possible break in the slope of the yield (see circle in Fig. 10(c)).

4.2.5. Critical energies E_2^0 and E_2^C

An important consequence of the present analysis is that the critical energy obtained under permanent irradiation, E_2^C, is below the critical energy E_2^0 obtained under a non-charging situation. This result is in opposition to a widespread opinion [30,55] following which the critical energy E_2^0 corresponds to a non-charging situation because $\delta + \eta = 1$. Present approach is supported by a rather large number of experiments where the critical energy, E_2^C, obtained under permanent irradiation ranges in the 1–3 keV interval for single crystal insulators where the critical energy obtained under non-charging measurements, E_2^0, is quite always larger than 10 keV. Among others there are experimental results on various alkali halides [55,56] and

of oxides such as MgO or Al_2O_3 [57–60]. The experimental investigation of a series of insulators, NaCl; MgO; SiO_2; Al_2O_3 and Si_3N_4 by Auger electron spectroscopy (AES) leads to slightly larger E_2^C values than those previously reported because a positive surface potential of a 1 eV may be admitted in AES but it has dramatic consequences on the SEE yield [61]. Additional experimental evidences are the reported SEE yield less than the unity at PE energies when a yield larger than the unity was expected in the investigation of MgO thin films [62] and the negative charging starting at $E_2^C \sim 1$ keV for amorphous SiO_2 [60].

The measured E_2^C values are reported in Table 1 where the difference with the extrapolated E_2^0 values may be pointed out: a difference larger for single crystals than for amorphous specimens as a consequence of the larger energetic interval between E_{max}^0 and E_2^0 for single crystals than for amorphous specimens such as BeO and SiO_2. From the tabulated values of '*s*', the E_2^C values calculated from Eq. (6) with $R \sim 3s$ are also shown. The agreement between calculated and experimental E_2^C values is quite good if it is observed that they concern insulators having the same chemical composition but probably different in their form, impurities and crystalline structure. The increase of E_2^C due to the field-assisted migration of holes in the depletion region [52] and the influence of a non-negligible evacuation current (see below) may explain the remaining difference between calculated and experimental E_2^C values.

4.3. Evacuation current I_{ev}

Up to now, the specimen current has been postulated to be negligible assuming implicitly that all the total charge Q, difference between electron injection and electron emission, was remaining into the insulating specimen. This postulate overestimates the charging effects and in particular the value of the surface potential, V_S. When charges in excess are evacuated to ground V_S is less than the value deduced from Eq. (11) and a longer time is needed to reach a steady state point is situated somewhere between the initial point I and point S (see point P in top of Fig. 10). Then greater is I_{ev} and closer to the initial point I is the steady state point P but its exact position may change with the fluence rate even for a constant fluence, $I^0 t_{irr}/S$ because a longer irradiation time, t_{irr}, permits a larger fraction of the mobile charge to be evacuated to ground [52].

In fact, a detailed calculation of the evacuation current I_{ev} is difficult. The complications result from the fact the total charge Q into the specimen is the sum of the trapped charge Q_T able to stay days or more into the specimen and a mobile charge, Q_M, that contributes to the evacuation current I_{ev} during and after irradiation. This evacuation current, itself, is the sum of the evacuation of free carriers existing prior the irradiation and of the evacuation of mobile charges induced by the irradiation. The contribution of the free carriers existing prior the irradiation is directly related to the DC conductivity, γ_o, of the investigated material and is the dominant term for conductors while the evacuation to ground for insulators may follow two different channels (inset Fig. 9): a bulk channel $I_{ev(s)}$ and a surface channel $I_{ev(b)}$ that may short-circuit the bulk channel [63,64]. It is then difficult to evaluate the fractions Q_T/Q and $I_{ev(s)}/I_{ev}$ because their values depend not only upon the chemical composition of the investigated specimen and of its electrical bulk parameters, ε_r and γ_0, but of its specific crystalline state, specific shape (dimensions) and specific surface conductivity as well as the quality of the electrical contact between the specimen and the specimen holder. For practical purposes the remaining strategy is to measure I_{ev} and $\partial Q/\partial t$ in independent measurements [53] but on a specimen similar to that where the SEE measurements are next performed.

4.4. Practical consequences and strategies

The main difficulty for predicting charging results from the fact that the knowledge of the chemical composition of the specimen is not sufficient and strategies have to be developed to identify and to minimize these spurious effects. To minimize charging effects, some strategies may be deduced from the plane capacitor approximation: $Q = CV_S$ with $C = \varepsilon S/h$ and they lead to increase C in order to decrease V_S for a given amount of charge Q. This increase may be obtained by increasing the irradiated area S from the increased defocusing of the incident beam more than by increasing an enlarged scanned area because, even scanned, a focused beam may induces a deficit in the SEE yield [52]. The increase of C may also be obtained by decreasing the thickness h of the specimen. The decrease of h down to the PE range R is particularly efficient because it also may open a new channel for the evacuation of the excess charges to the ground but care has to be taken to do not overcome the limit $h \sim 4R/10$. This limit corresponds to the maximum penetration depth of PE that may be next backscattered [37] and, when this limit is overstepped, the SEE yield is modified by the contribution of secondary electrons generated by the substrate backscattering coefficient $\eta_{substrate}$ instead of by the specimen backscattering coefficient $\eta_{specimen}$.

Another possibility is to optimize Q as a function of E^0. For instance, it is to choose a calculated Q value corresponding to the increase of V_S less than $V_C + 0.05$ V for a positive surface potential and $|V_S|$ less than 0.1 kV for a negative surface potential. In the energy range $E_1^0 < E^0 < E_2^0$, this strategy leads to shorten the dwell time, τ or $I^0\tau/S$, with respect to its value in the energy range $E^0 > E_2^0$. In addition, an increased dead time between the successive pulses or the decrease of the fluence rate, I^0/S, for a constant fluence, $I^0\tau/S$, permits the mobile charges Q_M to be more easily evacuated to ground. This solution is limited by the fact that the fraction Q_T remains a very long time into the specimen and the corresponding charges accumulate during all the duration of the experiment. To prevent such an accumulation at a given place, the need is to change randomly the places of the irradiated zone in

combination with the change of the dwell time. During the dead times, an alternative solution consists in detrapping the trapped charges by increasing the temperature of the specimen or in inducing a surface conductivity by an additional irradiation such as a large UV irradiation. Prior to the SEE yield measurement, it is also possible to test the ability to charge of the specific type of specimen of interest. Recently applied to a quartz crystal and an amorphous glass specimen such a test consists in the measurement of the influence current issued from a rear electrode, I_{inf}, not in ohmic contact with the specimen [53].

In fact the above strategies are often limited by the frequent co-existence of charging effects and of damaging effects. The damaging effects mainly result from electron-induced desorption of species such as oxygen in oxides and F or Cl in halides. Desorption effects lead to chemical modifications of the surface and then to the change of the SE escape probability but also to an increase of charging effects via the increase of atomic vacancies and then the density of trapping sites for the charges [65]. Then, the final strategy to be always applied is to control the reliability of the yield curves that have been experimentally obtained. In the context of the present paper, it is suggested to compare the RYC deduced from experiments to that calculated from the model and k value described in Section 3. When the fit between the two is good, one may be confident in the experimental results but charging artefacts may be suspected when the experimental k value is less than expected because charging effects distort more the SE yield curve in the energy range $E_1^0 < E^0 < E_2^0$ than in the energy range $E^0 > E_2^0$. This distortion is characterized by a flattening of the NYC (see Fig. 10(c)) and to a less k value than expected. This point is illustrated in Fig. 10(c) where a sudden change in the slope of the experimental RYC, also permits to suspect artefacts.

5. Conclusion

A compilation of experimental SEE yield data of uncharged inorganic insulators permits to observe that deviations between the various results obtained on a given compound defined by its chemical composition are far larger than the experimental uncertainties. Combined to the influence of surface treatments on the SE escape probability, the main reason is the dramatic influence of the structural disorder (crystalline state, dislocations, impurities, etc.) on the transport of SE prior to their emission into the vacuum. This experimental evidence makes pessimistic on the possibility to predict experimental yields results versus Primary energy, $\delta = f(E^0)$, obtained on practical specimens from the use of calculations, even sophisticated. Fortunately, it has been shown that experimental reduced yield curves, $\delta/\delta_{max} = f[E^0/E^0_{max}]$, are independent from SE attenuation length, s, and of SE escape probability, A, and are only dependent from the mean atomic number of the investigated specimen $\langle Z \rangle$. Then if no single (universal) reduced yield curve permits to fit the experiments obtained on very different materials, the use of a new model permits to predict the RYC of any compound from the knowledge of its $\langle Z \rangle$ value independently from any material constant such as s, A or ρ (mass density). This model is based on a more realistic physical description of the in-depth SE generation than that used in the standard model. It requires a single choice for exponent 'n' in an energy-range relationship instead of an arbitrary change of this exponent and it is also easy to operate with a desk top computer [66]. When the maximum values, δ_{max} and E^0_{max} are experimentally known, this model allows the experimentalists to extrapolate the measurements over a reasonably larger energy range (including the estimate of the critical energy E_2^0) and to extract interesting information on the investigated specimen such as the order of magnitude for the SE attenuation lengths, s, and SE escape probability, A. These applications have been illustrated for a significant number of metallic oxides and alkali halides and the resulting values have been discussed with a new estimate of A, $A \sim T(\beta = 0°) \times (1 - \cos\ \beta_1)$, that takes into account the effect of SE emission at oblique incidence and another illustration shows how to deduce the X-ray-induced secondary electron emission from the experimental electron-induced SEE and vice versa.

Resulting from a competition between electron injection and electron emission, the analysis of mechanisms of charging shows that their time dependence is mainly governed by the change of the SEE yield during irradiation and this change is characterized by a more rapid decrease of the SEE yield when the surface potential is positive than its increase when the surface potential is negative. The final result is a specific distortion of the SEE yield curve and a practical consequence is the possibility to suspect charging effects when the experimental RYCs do not fit that expected from the use of the new model. Another consequence is the need to shorten the pulse duration when the energetic interval $E_1^0 - E_2^0$ is explored. It is also shown that the steady state equilibrium not only requires $\delta^c(E) + \eta^c(E) = 1$ but also that the effective penetration range of the PE has to be nearly equals to the maximum escape depth of the SE (for facilitating the recombination of the electrons and holes being generated at this steady state). This constraint implies a critical energy being attained at the steady state, E_2^C, significantly different from the critical energy E_2^0 deduced from non-charging experiments: an analysis in contrast with a widespread opinion but supported by many experimental results. Finally, strategies to minimize the charging effects or at least to identify them have been suggested.

The present analysis of charging mechanism may be transposed to any technique based on incident electrons, such as Auger electron spectroscopy, because the causes of charging, SEE and excess of incident electrons, are the same even if the consequence may be different: a positive charging of say +1 V is negligible for the practical applications of e-AES and it has dramatic consequences in the measurement of the SEE yield.

Ignoring the radiation damage effects that are often correlated to charging effect and outlining the difficulty to predict the value of the evacuation current, I_{ev}, the present contribution cannot pretend to be complete and it is only hope that it may allow experimentalists to test easily the reliability of their results.

Acknowledgements

The author is deeply indebted to Dr. N. Hilleret (CERN, Geneva, Switzerland), Dr. O. Jbara (University of Reims, France) and Prof. E. Rau (Moscow State University; Russia) for their help in clarifying many practical aspects and to Dr. D.C. Joy (University of Tennessee) for his very useful data base [23].

References

[1] A.J. Dekker, Secondary Electron Emission Solid State Phys. 6 (1958) 251.
[2] O. Hachenberg, W. Brauer, in: L. Marton (Ed.), Advances in Electronics and Electron Physics, Vol. XI, Academic Press, NY, 1959, p. 413.
[3] H. Seiler, J. Appl. Phys. 54 (1983) R1.
[4] K. Kanaya, S. Ono, F. Ishigaki, J. Phys. D: Appl. Phys. 11 (1978) 2425.
[5] K.I. Grais, A.M. Bastawros, J. Appl. Phys. 53 (1982) 5239.
[6] H. Fujii, Y. Shibuya, T. Abe, R. Kasai, H. Nishimoto, J. Spacecraft Rockets 25 (1988) 156.
[7] H. Kimura, I. Mann, Earth Planets Space 51 (1999) 1223.
[8] D.C. Joy, C.S. Joy, J. Microsc. Soc. Am. 1 (1995) 109.
[9] J.P. Ganachaud, M. Cailler, Surf. Sci. 83 (1979) 498.
[10] S. Ichimura, R. Shimizu, Surf. Sci. 197 (1981) 386.
[11] J.C. Kuhr, H.J. Fitting, J. Electron Spectrosc. Rel. Phen. 105 (1999) 257.
[12] Z.J. Ding, D. Tang, R. Shimizu, J. Appl. Phys. 89 (2001) 718.
[13] H. Salow, Phys. Z. 41 (1940) 434.
[14] G.F. Dionne, J. Appl. Phys. 46 (1975) 3377.
[15] D.C. Joy, J. Microsc. 147 (1986) 51.
[16] B. Petzel, Thesis Dresden (1958) also reported in [2].
[17] N.R. Whetten, J. Appl. Phys. 35 (1964) 3279.
[18] N.R. Whetten, A.B. Laponski, J. Appl. Phys. 30 (1959) 432.
[19] Y. Ushio, T. Banno, N. Matuda, Y. Saito, S. Baba, A. Kinbara, Thin Solid Films 167 (1988) 299.
[20] J.B. Johnson, K.G. McKay, Phys. Rev. 91 (1953) 582.
[21] P.H. Dawson, J. Appl. Phys. 37 (1966) 3644.
[22] J.E. Yater, A. Shih, R. Abrams, Appl. Surf. Sci. 146 (1999) 341.
[23] D.C. Joy, update data available at <http://pciserver.bio.utk.edu/metrology>.
[24] Y.C. Yong, J.T.L. Thong, J.C.H. Phang, J. Appl. Phys. 84 (1998) 4543.
[25] H.J. Hopman, H. Alberda, I. Attema, H. Zeitjlemaker, J. Verhoeven, J. Electron Spectrosc. Rel. Phen. 131–132 (2003) 51.
[26] C.A. Pintao, R. Hessel, J. Appl. Phys. 88 (2000) 478.
[27] H. Salow, Z. fuer Techni. Physik 21 (1940) 1.
[28] C. Bouchard, D. Carette, Surf. Sci. 100 (1980) 241.
[29] J. Cazaux, J. Appl. Phys. 89 (2001) 8265.
[30] L. Reimer, in: Scanning Electron Microscopy, Springer Series in Optical Science, Vol. 42, Springer Verlag, Berlin, 1985, p. 128.
[31] H.J. Fitting, Phys. Stat. Solidii A 26 (1974) 525.
[32] K. Kanaya, H. Hawakatsu, J. Phys. D: Appl. Phys. 5 (1972) 1727.
[33] N. Croitoru, A. Seidman, K. Yassin, Thin Solid Films 116 (1984) 327.
[34] E.O. Burke, IEEE Trans. Nucl. Sci. NS-27 (1980) 441.
[35] M. Salehi, E.A. Flinn, J. Phys. D: Appl. Phys. 13 (1980) 281.
[36] G.D. Archard, J. Appl. Phys. 32 (1951) 1505.
[37] H. Niedrig, J. Appl. Phys. 53 (1982) R15.
[38] J. Cazaux, J. Phys. D: Appl. Phys. 38 (2005) 2433.
[39] J. Cazaux, J. Phys. D: Appl. Phys. 38 (2005) 2442.
[40] J. Schou, Phys. Rev. B 22 (1980) 2141.
[41] I.M. Bronstein, B.S. Fraiman, in: Vtorichnaya Elektronnaya Emissiya, Nauka, Moskva, 1969, p. 340, also reported in [23].
[42] K. Kanaya, S. Ono, J. Phys. D: Appl. Phys. 11 (1978) 1495.
[43] P. Hesto, in: G. Barbottin, A. Verpaille (Eds.), Instabilities in Silicon Devices, Elsevier N H Amsterdam Pub., NY, 1986, p. 263.
[44] R.C. Alig, S. Bloom, C.W. Stuck, Phys. Rev. B 22 (1980) 5565.
[45] R.A. Baragiola, M. Shi, R.A. Vidal, C.A. Dukes, Phys. Rev. B 58 (1998) 13212.
[46] B.L. Henke, J. Liesegang, S.D. Smith, Phys. Rev. B 19 (1979) 3004.
[47] J. Llacer, E.L. Garwin, J. Appl. Phys. 40 (1969) 2766.
[48] D. Liljequist, Nucl. Instr. and Meth. B 142 (1998) 295.
[49] J. Cazaux, Thin Solid Films 434 (2003) 303.
[50] J. Cazaux, Y. Bozhko, N. Hilleret, Phys. Rev. B 71 (2005) 35419.
[51] W.J. Veigelé, X-ray cross section compilation, Defense Nuclear Agency report No. 243, Kaman Science Corp., Colorado Springs, Co. 80907, 1971.
[52] J. Cazaux, Scanning 26 (2004) 181.
[53] S. Farkhfakh, N. Ghorbel, O. Jbara, S. Rondot, D. Martin, Z. Farkhfakh, A. Kallel, J. Phys. D: Appl. Phys. 37 (2004) 2181.
[54] O. Paulhe, D. Juvé, D. Treheux, in: G. Damamme (Ed.), Proceedings of the 4th International Conference on Electric Charges in non-conductive Materials, Tours, France, July 2001, Societé Francaise du Vide, Paris, Special Issue of Vide (2001) 330.
[55] L. Reimer, U. Golla, R. Bongeler, M. Kassens, B. Schindler, R. Senkel, Optik 92 (1992) 14.
[56] R. Bongeler, U. Golla, M. Kassens, L. Reimer, B. Schindler, R. Senkel, M. Spranck, Scanning 15 (1993) 1.
[57] J. Moller, J.P. He, Nucl. Instr. and Meth. B 17 (1986) 137.
[58] H. Guo, W. Maus-Friedrichs, V. Kempter, Surf. Interf. Anal. 25 (1997) 390.
[59] M. Belhaj, O. Jbara, M.N. Filippov, E.I. Rau, M.V. Andrianov, Appl. Surf. Sci. 177 (2001) 58.
[60] C.H. Seager, W.L. Warren, D.R. Tallant, J. Appl. Phys. 81 (1997) 7994.
[61] M.P. Seah, S.J. Spence, J. Electron Spectrosc. Rel. Phen. 109 (2000) 291.
[62] J.J. Scholtz, R.W.A. Schmitz, B.H.W. Hendriks, S.T. de Zwart, Appl. Surf. Sci. 111 (1997) 259.
[63] H.J. Wintle, J. Appl. Phys. 81 (1997) 2682.
[64] Z.G. Song, C.K. Ong, H. Gong, Appl. Surf. Sci. 119 (1997) 169.
[65] J. Cazaux, J. Electron Spectrosc. Rel. Phen. 105 (1999) 155.
[66] Free EXCEL files available on request at: jacques.cazaux@univ-reims.fr.